Elastic volume reconstruction from series of ultra-thin microscopy sections

Saalfeld, Stephan ; Fetter, Richard ; Cardona, Albert ; Tomancak, Pavel

Abstract: Anatomy of large biological specimens is often reconstructed from serially sectioned volumes imaged by high-resolution microscopy. We developed a method to reassemble a continuous volume from such large section series that explicitly minimizes artificial deformation by applying a global elastic constraint. We demonstrate our method on a series of transmission electron microscopy sections covering the entire 558-cell Caenorhabditis elegans embryo and a segment of the Drosophila melanogaster larval ventral nerve cord.

DOI: https://doi.org/10.1038/nmeth.2072

Elastic Volume Reconstruction from Series of Ultra-thin Microscopy Sections

Stephan Saalfeld[1], Richard Fetter[2], Albert Cardona[3,2], & Pavel Tomancak[1]

[1]Max Planck Institute of Molecular Cell Biology and Genetics, Pfotenhauerstraße 108, Dresden, Germany
[2]Janelia Farm Research Campus, Howard Hughes Medical Institute, Ashburn, Virginia, USA
[3]Institute of Neuroinformatics, Uni/ETH Zurich, Winterthurerstrasse 190, Zürich, Switzerland

Correspondence should be addressed to: tomancak@mpi-cbg.de and acardona@ini.phys.ethz.ch

Anatomy of large biological specimens is often reconstructed from serially sectioned volumes imaged by high resolution microscopy. We developed a method to re-assemble a continuous volume from such large section series that explicitly minimizes artificial deformation by applying a global elastic constraint. We demonstrate our method on a series of Transmission Electron Microscopy sections covering the entire 558 cell *Caenorhabditis elegans* embryo and a segment of the *Drosophila* larval ventral nerve cord.

Serial section microscopy is a classic technique for detailed anatomy reconstruction of large biological specimens. Typically, the fixed specimen is embedded in a block of solid medium and then cut into a series of ultra-thin sections. Sections are collected, mounted, individually stained and imaged. Using ultra-thin sections effectively eliminates the penetration problem for both staining and imaging. Furthermore, the minimum achievable section thickness at less than 40 nm is a significant improvement over the axial resolution that can be achieved by optical sectioning techniques as Confocal Laser Scanning Microscopy. Sections can be imaged as mosaics of overlapping image tiles, either manually or using a motorized stage, allowing the imaging of very large fields of view. In combination, these advantages render serial section microscopy particularly useful for large scale high resolution reconstructions, for example, of dense neuronal tissue, where the method employing Electron Microscopy (EM) recently experienced a renaissance[1-6].

The downside of the method is that by physically cutting a block into sections the continuity between sections is lost and individual sections are deformed. To recover the imaged volume and extract biologically interesting information such as the reconstruction of neuronal circuits[2,3,5], sections need to be aligned and distortion must be removed. Alignment can be achieved by maximizing the overlap of similar image content between adjacent sections. However, there are two unknowns that change image content across the section series: specimen's shape and independent section distortion introduced during preparation. Naively warping one section into another would compensate for the shape of the specimen and by that introduce artificial deformation. Our method exploits the fact that the biological specimen's shape typically changes smoothly across sections whereas the independent distortion in each section is random and uncorrelated with neighboring sections. We align all sections not only to their direct neighbors in the series

but to all sections in a local neighborhood by modelling sections as two-dimensional elastic sheets that penalize non-rigid deformation (**Fig. 1a** and **Supplementary Fig. 1**). All sections are treated as moving targets in a template-free global alignment. The elastic constraint is implemented as a spring-connected particle system where each section is represented as a triangular spring-mesh (**Fig. 1b** and **Supplementary Video 1** and **Online methods**).

For each vertex of the spring-mesh, we search for the corresponding location in other sections by pairwise block-matching using normalized cross-correlation (NCC). To that end, we explore all translation vectors in an immediate neighborhood which requires sections to be in approximate alignment (**Fig. 1c,d**). We estimate this approximate alignment using automatically extracted landmark correspondences from invariant local image features as described previously[7,8]. Originally proposed for robust object recognition under partial occlusion, this method can deal with significant non-linear distortion and image artifacts that inevitably occur in large section series (**Supplementary Fig. 2**). Both matching local image features and matching local blocks create a substantial number of spurious matches that would impair alignment and introduce artificial deformation. We effectively remove such spurious matches using a set of filters that include local properties of features and block matches as well as global geometric constraints imposed by the supported transformation (**Fig. 1e,f** and **Supplementary Fig. 3** and **Online Methods**). The ratio of matches passing the filters constitutes a deformation invariant similarity metric for two sections that can be used to correct the order of the series or to estimate the number of missing sections (**Supplementary Fig. 4**).

All vertices for which corresponding locations in other sections could be identified are connected by zero-length springs to those sections (**Fig. 1a,b**). The distance in a series to which cross-section connections spread is limited by how rapidly the biological structure changes across sections (for ~50 nm Transmission Electron Microscopy section series (ssTEM) it is typically 7±5 sections). Springs across and within sections serve concurrent purposes; while cross-section connection support series alignment, springs in the triangle mesh within sections tend towards maintaining a rigid transformation of the sections and penalize distortion. Relaxing this system leads to a series of smoothly aligned sections with the required non-rigid deformation distributed

equally among all sections. That is, for each individual section, the deformation relative to a rigid transformation is explicitly minimized (**Supplementary Fig. 5**). Only by this constraint, arbitrarily large section series can be aligned without propagating transformation errors. Similarly to elastically aligning a series of deformed serial sections, our method can be used to assemble montages from deformed overlapping image tiles covering a single section (**Supplementary Fig. 6**). Taken together, a single framework enables montaging and alignment of massive series of tiled sections.

Similar elastic constraints have been proposed earlier[9,10], combining search for an elastic alignment and a pixel-based pairwise similarity estimate between adjacent sections in an iterative solution. They propose initial linear pre-alignment of the section series based on variants of principal component analysis. Our method differs in four key areas: Firstly, we compare and align not only adjacent sections but all sections in a local neighborhood (**Fig. 1a** and **Supplementary Fig. 1**). Secondly, we use invariant local image features[7] to calculate an initial approximate alignment[8] (**Fig. 1c**). Thirdly, we separate pairwise correspondence search from the elastic alignment, yielding an efficient solution for even very large data (**Fig. 1d**). Fourthly, we implemented a set of filters to robustly exclude staining artifacts and otherwise corrupted image regions from contributing to the alignment (**Fig. 1e** and **Supplementary Fig. 3**). In order to evaluate our method quantitatively we generated synthetic volumes that mimic the properties of biological tissue, sectioned them and introduced artificial deformation to the sections. We measured the alignment error using a sample of straight lines projected through the volume along the *z*-axis. The elastic method outperforms rigid and affine alignment in its ability to recover the straight lines (**Supplementary Figs. 7–12** and **Supplementary Videos 2** and **3**).

We applied our method to two large ssTEM data sets (**Supplementary Table 1**) using a standard quad-core desktop computer with 24 gigabytes of memory. The first data set is a series showing an entire three-fold stage *Caenorhabditis elegans* embryo. 803 sections of 50 nm thickness were scanned from film negatives at a size of 6,160×4,640 pixels resulting in a resolution of 4 nm per pixel (**Fig. 2a**). The series was pre-aligned rigidly followed by elastic alignment exploring a neighborhood of up to 6 sections for each section. The elastic method dramatically improves the alignment both in terms of overall specimen outer shape and the internal structure (**Fig. 2c** and **Supplementary**

Videos 4–7). We made the result available for interactive exploration at various scales in CATMAID[11] (*http://fly.mpi-cbg.de/c-elegans)***.**

The second data set is an approximately transversal series through an abdominal segment of the ventral nerve cord of a *Drosophila melanogaster* first instar larva (**Supplementary Fig. 13)**. The series consists of 458 sections at 45 nm thickness, each imaged as a mosaic of more than 70 overlapping image tiles (altogether 33,051 images) of 2,048×2,048 pixels covering a canvas of about 22,000×17,000 pixels at a resolution of 4 nm per pixel (**Fig. 2b**). TEM sections experience heat-induced deformation during image acquisition, which resulted in displacements of up to 50 pixels when only a rigid transformation was used to stitch the montages (**Supplementary Fig. 6**). Consequently, this data set was aligned in two elastic alignment steps: firstly, all sections were elastically montaged and secondly, the series of montages was elastically aligned exploring a neighborhood of up to 8 sections. Contrary to the *C. elegans* data set, we initialized the elastic series alignment with the result of a previously developed, automatic landmark-based method[8] instead of a rigid alignment. Similarly to the *C. elegans* dataset we observed dramatic improvement of the alignment after the elastic method was applied both in terms of the ventral nerve cord's outer shape and the internal structure down to the resolution sufficient for distinguishing individual synapses in the axial direction (**Fig. 2d, e, Supplementary Fig. 14** and **Supplementary Videos 8–11**).

To further substantiate the benefits of our elastic alignment method for recovering the biological shape of the imaged specimen, we traced several individual neurons from their cell bodies to the neuropil where they branch and engage in synaptic connections. Tracing was performed manually, using the TrakEM2 software[12], on a previous version of the dataset aligned using manually corrected sequential affine transformations comparable in quality to the rigid alignment shown in this manuscript. The manual traces were computationally transferred into the elastically aligned dataset and visualized (**Figs. 3a–d**). While rigid alignment suffers from characteristic jitter of traced neuronal profiles, the elastically aligned dataset is smooth, better reflecting shape details of the biological tissue. Jitter from insufficient alignment contributes significantly to the total length of skeleton traces. Elastic alignment reduces the total skeleton length of the neuronal arbors shown in **Fig. 3** from 2.87 mm in the rigidly aligned series and 1.55 mm

using our previous method[8] to 1.25 mm which approaches the lower bound length of the skeleton graph of 0.95 mm (**Supplementary Fig. 15** and **16**). The ability to extract better axonal shapes will aid in the comparison of EM and light microscopy data for neuronal circuit reconstruction at vastly different scales[3,13].

We have implemented our elastic alignment method in the Java programming language on top of the popular image processing program ImageJ. The method is available through two standalone ImageJ-plugins (for creating montages and series alignment) and embedded in the registration and annotation toolkit TrakEM2, where it is complemented by other registration, segmentation and data mining tools[12]. The method is released as Open Source under the General Public License and distributed through the ImageJ distribution Fiji[14] (**Supplementary Note**). In principle it can be applied to reconstruct any large serial section dataset such as array tomography[15](**Supplementary Videos 12–14** and **Supplementary Note**). These properties make this method ideally placed for application to emerging and future challenges in high-resolution reconstruction of large biological specimens imaged as series of physical sections.

Acknowledgements

We thank C. Bargmann, Rockefeller University, for making the *C. elegans* data available and F. Collman, N. Weiler, K. Micheva and S. Smith, Stanford University, for sharing the exemplary Array Tomography dataset. We thank T. Pietzsch for insightful discussion of algorithmic details and S. Grill for helpful comments on the manuscript. We thank D. Berger and I. Arganda for inspiration on regularized affine series alignment. S.S. was funded by DIGS-BB, P.T. was funded by MPI-CBG. R.F. is supported by HHMI. A.C was funded by the Institute of Neuroinformatics, U. Zurich and ETH Zurich. A.C thanks J. Simpson and the Visitor Program at HHMI Janelia Farm.

Author Contributions

S.S. and A.C. conceived the research and analyzed the data. S.S. designed the algorithms and wrote the software. R.F. and A.C. collected image data. A.C. reconstructed neuronal arbors. S.S. and P.T. wrote the paper with input from co-authors.

COMPETING FINANCIAL INTERESTS

No competing financial interests declared.

References

1. Hayworth, K. J., Kasthuri, N., Schalek, R. and Lichtman, J. W. *Microscopy and Microanalysis*, 12(Suppl. 02):86–87, (2006).
2. Anderson, J.R. et al. *PLoS Biology*, 7(3):e1000074, 03 (2009).
3. Cardona, A. et al. *PLoS Biology*, 8(10):e1000502, (2010).
4. Chklovskii, D.B., Vitaladevuni S. and Scheffer L.K. *Curr Opin Neurobiol*, 20(5):667–75, (2010).
5. Bock, D.D. et al. *Nature*, 471:177–182, (2011).
6. Briggman, K.L. and Bock, D.D. *Curr Opin Neurobiol*, In Press (2011).
7. Lowe, D.G. *International Journal of Computer Vision*, 60(2):91–110, (2004).
8. Saalfeld, S., Cardona A., Hartenstein V. and Tomancak P. *Bioinformatics*, 26(12):i57–i63, (2010).
9. Guest, E. and Baldock, R. *Bioimaging*, 3(4):154–167, (2001).
10. Schmitt, O, Modersitzki J., Heldmann S., Wirtz S. and Fischer B. *International Journal of Computer Vision*, 73(1):5–39, (2007).
11. Saalfeld, S., Cardona A., Hartenstein V. and Tomancak P. *Bioinformatics*, 25(15):1984–1986, (2009).
12. Cardona, A. et al. *PLoS ONE* (2012, in press).
13. Cardona, A. et al. *J Neuroscience*, 2;30(22):7538–53, (2010).
14. Schindelin, J. et al. *Nature Methods* (2012, in press).
15. Micheva, K.D. and Smith, S.J. *Neuron* 55:25–36, (2007).

Online methods

The elastic model

We achieve globally minimized deformation by modelling alignment as a two-dimensional elastic system of vertices connected by ideal springs according to Hooke's law. A Hookeian spring has a relaxed length at which it exerts no force. Both extending and compressing a Hookeian spring results in increasing stress. The stress amplitude is proportional to the difference of the spring's actual length and its relaxed length. Springs connecting the vertices of an 'image-mesh' have a relaxed length corresponding to the distance of the vertices in the non-deformed image. Deforming the image-mesh compresses and extends springs and therefore results in stress. Hooke's law enables to model springs with a relaxed length of zero for which no physical equivalent exists. A zero-length spring exerts force proportional to its extension beyond zero-length, it cannot be compressed. Zero-length springs can be used to connect points that should be positioned at the same location. We connect corresponding locations between two overlapping images (tiles in a montage or sections in a section series) by zero-length springs. These springs aim to warp the images towards perfect overlap. In contrast, the non-zero length springs within image-meshes prefer a locally rigid transformation of each image. That way, the system penalizes arbitrary warp and distributes deformation evenly among all images.

Each image is tessellated into a mesh of regular triangles with each vertex being connected to its neighboring vertices by a spring whose relaxed length is the original edge length of the triangle (**Fig. 1b** and **Supplementary Note**). For those vertices of the mesh on image I_1 overlapping image I_2, we identify their corresponding location in image I_2 by block matching. The vertex is then connected into the mesh on image I_2 by a zero-length spring with its target end being located at an arbitrary place inside a triangle of the target mesh. Note that this 'passive' end does not contribute to the deformation of the mesh on image I_2 because it is not connected to any of its vertices by a spring. During relaxation, its location is updated according to the affine transformation defined by the three vertices of the embedding triangle. Vice versa, vertices of the mesh on image I_2 are connected to their corresponding location in image I_1 with their 'passive' ends updated according to the affine transformation of the embedding triangle in the mesh on

image I_1.

The stiffness of ideal Hookeian springs is specified by the spring constant k. Increasing the spring-constant for springs spanning the triangle-mesh will lead to less deformed images and also less well aligned solutions. Using too small spring-constants effectively eliminates the elastic constraint and will therefore result in arbitrarily warped solutions. We have empirically estimated a spring-constant k = 0.1 being appropriate for our TEM series. During series alignment, the spring-constant for cross-section springs depends on the index distance d in the series (k = 1/d) giving farther sections less impact.

We relax the elastic system using an iterative solution similar to gradient descent. The desired end-state of the system is where for each vertex the forces of all attached springs combine to zero. The force vector F for a vertex v_0 can be calculated using Hooke's law (**Equation 1** and **Supplementary Fig. 5**).

$$\vec{F} = -\sum_{i \in \{1 \ldots n\}} k_i \vec{x}_i \quad \text{with} \quad \vec{x}_i = \left(1 - \frac{l_i}{|\vec{p}_i - \vec{p}_0|}\right)(\vec{p}_i - \vec{p}_0) \tag{1}$$

At each iteration, force vectors are calculated for all vertices and then all vertices are moved alongside their force vector. The distance of the move is the length of the force vector divided by the length of the largest force vector in the entire system. That way, the maximum step size per iteration is one pixel. All 'passive' spring ends are moved according to the affine transformation specified by the embedding triangle, preserving their relative location in the triangle. The solution typically converges within a few hundred iterations.

Matching corresponding image content

Our method incorporates two techniques for establishing pairwise correspondences (p,q) between a point p in an image I_1 and a point q in an image I_2: (1) matching invariant local image features and (2) matching blocks. Invariant local image features are used to establish sparse sets of corresponding landmarks between two images for which an approximate alignment is not known. We use the popular Scale Invariant Feature

Transform[7] (SIFT) for interest point detection and feature matching. An approximate alignment for pairs or groups of overlapping images can be established by least-squares fitting an appropriately simplified transformation model (e.g. a rigid transformation for each section, see **Fig. 1c**) to corresponding landmarks. In a previously published method[8], we estimate the optimal rigid transformation for each individual tile of a large tiled section series simultaneously. Each tile connects to overlapping tiles within the section and across the series. While not compensating for low scale deformation and delivering insufficiently stitched montages, the method can serve as a very good initialization for elastic montaging and series alignment of such datasets. We have extended this method to estimate an affine transformation per each tile that is regularized with respect to a rigid transformation which effectively prevents arbitrary shear and scaling while better compensating for non-rigid deformation (**Supplementary Note**).

Block matching is performed on the approximately pre-aligned images. The local vicinity around each vertex of the section spring-mesh is inspected for an optimal match. We use the normalized cross-correlation (NCC) coefficient *r* of a patch around the vertex and the overlapping patch in the other image as quality measure for a match. The location with maximal *r* specifies the offset of the vertex relative to the initial linear alignment. Block matching is executed on reasonably down-scaled versions of the images. The ideal scaling factor depends on the application and quality of the signal. In our ssTEM series, the disparity between lateral and axial resolution suggests a scaling factor of 0.1 by which isotropic resolution is achieved. To overcome the reduced accuracy of the estimated offset, we use Brown's method[16] to calculate an approximate sub-pixel offset.

Filtering spurious matches

Both image feature matching and block matching are local methods and can generate false positives. We reject those with a set of filters that exploit local (**Supplementary Figure 3**) and global properties of the matches.

Correlation threshold: block matches with an NCC coefficient r below a user specified threshold are rejected (Supplementary Figure 3c). The NCC coefficient ranges from -1.0 to 1.0 with r = 1.0 indicating perfect linear dependency, r = 0.0 indicating no linear

dependency and r = -1.0 indicating inverse linear dependency.

Edge responses: block matches as well as interest points for feature detection may be detected on top of elongated structures (edges, ridges, stripes) and therefore poorly localized alongside the structure (Supplementary Figure 3d,f). Such detections have a large (orthogonal to the ridge) and a small (alongside the ridge) principal curvature and can thus be identified by a large ratio between the two values[7]. Detections with a ratio larger than a given threshold are rejected.

Ambiguous matches: for feature descriptor matching, Lowe proposed to compare the distances of the reference to the second best and best match[7]. For a distinctive true match, the ratio between the two distances is most likely significantly lower than 1.0 whereas for a wrong match, many matches are expected to have very similar distances leading to a ratio close to 1.0. During block matching, we use the filter to reject matches where multiple offsets result in similar correlation (**Supplementary Figure 3e,f**).

Geometric consensus: using local methods exclusively will either lead to false positives being accepted when using too soft constraints or many correct matches being rejected by using too hard constraints. We therefore use the consensus of matches that were filtered by moderate local filters to reject the remaining outliers. The methods used are the Random Sample Consensus[17] (RANSAC) and two variants of robust regression. All three methods make use of the observation that the hidden transformation is supported by all true matches up to an approximately normal distributed transfer error whereas wrong matches do not support a common transformation. RANSAC identifies a hidden transformation by counting the supporting matches for many hypotheses generated from random minimal samples. If the minimal sample contains only true positives then the hypothesis will be supported by all true positives. The best hypothesis is that with the highest number of supporters. RANSAC is very effective to separate a small fraction of correct matches from a large set of false positives but leaves open where to put the threshold for accepting a match as a supporter. That gap is closed by using a robust regression estimator that combines a least-squares estimator with an outlier filter based on error statistics in an iterative loop. It very effectively removes moderate fractions of outliers while automatically estimating the required threshold.

Feature matches are filtered using RANSAC followed up by robust regression for a simple linear transformation model[8]. Block matches are filtered using another variation of robust regression. Each match (p_0,q_0) is inspected individually for being an outlier. To that end, all other block matches (p_i,q_i) are used to estimate a linear transformation T (e.g. an affine transformation) by means of weighted least squares with each match (p_i,q_i) being weighted by a Gaussian radial distribution function (RDF) ω centered at the reference (p_0,q_0) (**Equation 2**).

$$\arg\min_{T} \sum_{i \in \{1 \ldots n\}} \omega_i \left| T(\vec{p}_i) - \vec{q}_i \right|^2 \quad \text{with} \quad \omega_i = e^{\frac{\left|\vec{p}_i - \vec{p}_0\right|}{-2\sigma^2}}$$

(2)

Choosing a larger standard deviation σ for the RDF ω requires the deformation field to be smoother. A match is rejected if its transfer error with respect to T is larger than a given threshold or if it is larger than k times the average transfer error. The average transfer error is accumulated from all matches weighted by the RDF ω accordingly. The filter is applied in a loop until no match had been removed.

Naturally, the fraction of correct matches degrades with increasing distance of two sections in the series. It can therefore be used as a coarse deformation invariant distance metric to correct ordering mistakes and to estimate the approximate size of gaps in the series (**Supplementary Fig. 4**).

Manual skeleton traces

Jitter as introduced by insufficient alignment increases the total length of skeleton traces. We therefore report the scale-normalized total length l of the skeleton traces shown in **Fig. 3** as an alignment quality criterion (**Equation 3** and **Supplementary Fig. 15**).

$$l = \sum_{\forall(\vec{p},\vec{q})} \sqrt{\frac{(p_x - q_x)^2 + (p_y - q_y)^2}{s^2} + (p_z - q_z)^2}$$

(3)

The total length l is the sum of all edge lengths. All edge lengths ($|p,q|$) are normalized

by a local scale factor *s* that is the average scale factor of the contributing sections. The scale factor of a section is the average scale factor of all image tiles in the section and the scale factor of an image tile is estimated through a least-squares approximation of its non-linear elastic transformation by a similarity transformation (scale, rotation, translation). Shorter total length *l* implies improved alignment. Scale normalization makes the length measure invariant to global scaling. Without scale normalization, globally reducing the size of all (or a range of) sections would reduce the total length and render its applicability as a quality criterion for alignment useless. Elastic alignment decreases *l* by 56.4% compared with a rigid series alignment and by 19.1% compared with our previous method[8].

We compare the scale-normalized skeleton length *l* with a lower bound length *f*. The lower bound length *f* is the skeleton length of the skeleton after all edges between branch- and end-points have been replaced by straight lines (**Supplementary Fig. 16**). Since now only branch and end points suffer from alignment errors, the lower bound length *f* is robust with respect to insufficient section-to-section alignment. This robustness is reflected in the observation that elastic alignment decreases *f* by only 4.8% compared with a rigid series alignment and 0.7% compared with our previous method[8]. On the other hand, the percentual difference between *l* and *f* serves as an indicator for overall alignment quality. It is reduced to 31.8% by elastic alignment, compared to 188.0% for the rigid series alignment and 61.7% for our previous method[8] demonstrating the superior alignment results achieved by the elastic method. It is important to note that jitter in the manually generated skeleton-traces comes not solely from insufficient alignment but as well from inaccurate manual operation. This is particularly relevant for the annotations used in this paper since they were performed on poorly aligned data and annotation speed had a higher priority than accurate localization of each profile's center point. Our prediction is therefore that these skeleton traces cannot be used to report qualitative improvement over the current series alignment because the manual error already outweighs the alignment error.

Artificially generated ground truth

As suggested earlier[8], we have quantitatively evaluated the accuracy of our elastic alignment method using artificially generated ground truth. Using the Open Source Raytracer POVRay (http://www.povray.org/), we have generated a synthetic volume that

has the shape of a distorted ball filled with volumetric texture that resembles membranes and blob-like structures as present in biological tissue. We have artificially sectioned the volume at a section thickness of 2 pixels and generated two series of 400 sections, each 2,000×2,000 pixels. Evaluation series A repeats the same section 400 times (**Supplementary Video 2**). In this series, texture displacement is the exclusive result of deformation since no 'biological' signal changes alongside the *z*-axis. Evaluation series B consists of 400 serial sections including the signal change induced by the volume (**Supplementary Video 3**) and as such is a more realistic test case. We have artificially distorted all sections of both series using randomized smooth non-linear transformations using a Moving-Least-Squares affine transformation[18] for four control points at random source locations in either of the four quadrants of the image displaced by a maximum distance of 50 pixels. That induced section-to-section pairwise local deformation of up to 200 pixels relative to a rigid least-squares approximation. Each section was then rotated by a random angle and shifted in a random direction by up to 150 pixels. Both evaluation series were aligned using a rigid transformation per section, a regularized affine transformation per section (**Supplementary Note**) and our elastic alignment method on top of the affine alignment.

We report the average scale factor of each section relative to ground truth for all three alignment methods (**Supplementary Fig. 7**). Rigid series alignment per definition preserves the average section scale that has been introduced by non-linear deformation. Both affine and elastic alignment recover the original scale of all sections across the entire series. The elastic method performs better as it can compensate for non-linear deformation.

We compare alignment precision using a sample of straight lines projected along the *z*-axis through the ground-truth series. Ideally, these linesshould be reconstructed as straight lines along the *z*-axis. Only points covered by the 'specimen' are considered because background is not expected to and does not need to be aligned. For all lines, we report the absolute displacement in the *x*,*y*-plane relative to ground truth (**Supplementary Fig. 8–10**) and section-to-section pairwise displacement (**Supplementary Fig. 11–12**) in each *z*-section . Ground truth and reconstruction result were previously aligned by a 2d-rigid transformation to compensate for a global rotation and translational offset. Elastic alignment clearly outperforms rigid and affine alignment

in its ability to recover the original shape of the ‘specimen’ while at the same time effectively removing section to section jitter.

References

16. Brown, M. and Lowe, D.G. *BMVC*:656–665 (2002).
17. Fischler, M.A. and Bolles, R.C. *Comm. of the ACM* **24**(6):381–395 (1981).
18. Schaefer, S., McPhail T. and Warren J. *ACM Transactions on Graphics* **25**(3):533–540 (2006).
19. Ito, K., Urban, J. and Technau, G.M. *Roux’s Archiv of Dev. Biol.* **204**:284–307, (1995).

Figure Legends

Figure 1 | *The elastic alignment method.* (**a**) All sections in the series are aligned to not only their direct neighbors but to all sections in a local neighborhood. Sections are gray-coded to visualize how the influence of cross-section connections decreases in inverse proportion to the distance of the two sections in the series. That influence is specified by the spring constant. (**b**) Sections are modeled as elastic sheets by a two-dimensional spring connected triangle mesh.Springs within the mesh stabilize the section. Springs across sections are depicted by orange arrows. They have a relaxed length of zero and drag the sections towards alignment. (**c**) Corresponding landmarks in two adjacent sections that were established using local invariant features are connected by lines. These landmarks are used to calculate an initial approximate alignment and the remaining local deformation is estimated by block matching, here visualized by lines connecting the corresponding locations (**d**). (e) The resulting deformation field is displayed as color/intensity-encoded displacement vectors. Orientation/length scale (small colored circle) is blown up for better visualization. Spurious matches show up as outlier colors and are automatically rejected using local and global filters (**f**).

Figure 2 | *Reconstruction of two exemplary TEM section series.* Sections were scanned from film negatives (**a**,**b**) or assembled from many overlapping digital camera images (**c**,**d**,**e**) using our elastic alignment method in montaging mode. Parts of the reconstructed volumes are shown as arbitrarily sliced three-dimensional renderings (**a**,**c**). The planar resolution (scalebar, ~4 nm/pixel) is ~10× higher than the axial resolution (40–50 nm/section). The orientation of the section series is orthogonal to the horizontal plane (see staple). Specimens shown are a three-fold *Caenorhabditis elegans* embryo (803 sections; **a**,**b**) and 1.5 segments of the ventral nerve cord of a first instar *Drosophila melanogaster* larva (458 sections, each section consists of ~70 overlapping image tiles; **c**,**d**,**e**). (**e**) Image showing individual synapses in the orthogonally re-sliced volume. The Quick Response-code links to a collection of supplementary videos at http://fly.mpi-cbg.de/elastic.

Figure 3 | *Comparison of the reconstructed shapes of neuronal arbors using rigid series alignment and our elastic method.* Examplary neuronal arbor skeletons were manually

traced in the *Drosophila* series using the TrakEM2 software. The resulting shapes are compared for elastic (**a**,**b**) and rigid (**c**,**d**) series alignment. Traces are shown in two perspective projections: dorsal view (**a**,**c**) and lateral view from left to right (**b**,**d**). The section plane is orthogonal to the projection plane. Therefore, longitudinal branches expose jitter where alignment insufficiently compensates for low scale distortion (arrows and inset). Star marks a noticeable misalignment due to a gap of 5 lost sections (inset). Note that in the rigidly aligned series (**c**,**d**), this missalignment cannot be distinguished from general jitter.

Supplementary Material

Supplementary File	Title
Supplementary Figure 1	Comparison of elastic alignment exploring eight adjacent sections or only direct neighbors
Supplementary Figure 2	*Typical artifacts that inevitably occur in large TEM series*
Supplementary Figure 3	Local block matching filters
Supplementary Figure 4	The number of filtered matches can be used to detect artifacts and missing sections
Supplementary Figure 5	Spring forces
Supplementary Figure 6	Elastic montaging compensates for non-rigid deformation
Supplementary Figure 7	Comparison of average section scale factors after alignment of the evaluation series
Supplementary Figure 8	Histograms of absolute point displacements after alignment of evaluation series A and B
Supplementary Figure 9	Projection of the *x*,*y*-location of each *z*-point of a sample of straight lines projected through the volume along the *z*-axis
Supplementary Figure 10	Projection of the *x*,*z*-location of each *z*-point of a sample of straight lines projected through the volume along the *z*-axis
Supplementary Figure 11	Histograms of section-to-section pairwise point displacements after alignment of evaluation series A and B
Supplementary Figure 12	Visualization of section-to-section pairwise point displacements after alignment of evaluation series A and B
Supplementary Figure 13	Anatomical context of the *Drosophila* larval ventral nerve cord TEM section series
Supplementary Figure 14	Synapses are detectable in both lateral and axial views after elastic reconstruction
Supplementary Figure 15	Comparison of three alignment methods applied to the Drosophila series using the total length of manual skeleton annotation.
Supplementary Figure 16	Total skeleton length and lower bound skeleton length
Supplementary Table 1	Overview of reconstructed ssTEM datasets.
Supplementary Video 1	*Visualization of the behavior of spring meshes during elastic alignment.* The movie shows the iterative relaxation of the spring-particle system for five examplary serial sections from the *C. elegans* series. Sections were pre-aligned rigidly such that all section spring-meshes start from the same initial position. Zero-length cross-section springs connect all vertices to their corresponding location in other sections (except for those where no match could be found by block matching). Springs are displayed as lines with their color reflecting the relative stress

	applied. The color ranges from green (fully relaxed) to red (maximally stressed) and is scaled relative to the maximum stress present in the system. Initially, all intra-section-mesh springs are green and all cross-section springs are maximally stressed. After relaxation, stresses are distributed throughout the system. Cross-section springs have contracted and the series is warped into alignment.
Supplementary Video 2	*Evaluation Series A.* The movie shows Evaluation Series A. The series consists of 400 sections of 2,000×2,000px each, all sections showing the same artificially generated image. The original series has been deformed non-linearly and then aligned using a rigid or affine model per section (rigid, affine) and using our elastic method (elastic).
Supplementary Video 3	*Evaluation Series B.* The movie shows Evaluation Series B. The series consists of 400 sections from an artificially generated volume of 2,000×2,000×800 px. The section thickness is 2px. The original series has been deformed non-linearly and then aligned using a rigid or affine model per section (rigid, affine) and using our elastic method (elastic).
Supplementary Video 4	*Walk through the rigidly aligned C. elegans series.* The movie shows in each frame a single section from the rigidly aligned TEM section series of a *C. elegans* three-fold stage embryo at four different zoom levels (A–D where B shows the close up of the blue rectangled area in A etc.). The scale bars in each panel are 4 µm (A), 2 µm (B), 1 µm (C) and 0.5 µm (D). The lateral resolution of the raw data is 4 nm/pixel. The number in the upper right corner indicates the section index. Note the significant non-linear distortion remaining in the rigidly aligned series. A high resolution version of the movie can be downloaded from http://fly.mpi-cbg.de/elastic.
Supplementary Video 5	*Walk through the rigidly aligned C. elegans series orthogonally re-sliced.* The movie shows in each frame a single, computationally generated section orthogonal to the physical sectioning plane, through the rigidly aligned TEM section series of a *C. elegans* three-fold stage embryo. Sections were down-sampled such that their lateral resolution matches the section thickness of 50 nm/pixel. Accordingly, orthogonal sections are generated at a step-size of 50 nm. The number in the upper right corner indicates the virtual section index. Two different zoom levels are shown (A,B) where B corresponds to the blue rectangle in A. The scale bars in the panels are 5 µm (A) and 2 µm (B). Note the strong non-linear distortion remaining in the rigidly aligned series that effectively prevents identification of biologically relevant features in the axial direction. A high resolution version of the movie can be downloaded from http://fly.mpi-cbg.de/elastic.
Supplementary Video 6	*Walk through the elastically aligned C. elegans series.* The movie shows in each frame a single section from the elastically aligned TEM section series of a *C. elegans* three-fold stage embryo at four different zoom levels (A-D where B shows the close up of the blue rectangled area in A etc.). The scale bars in each panel are 4

	µm (A), 2 µm (B), 1 µm (C) and 0.5 µm (D). The lateral resolution of the raw data is 4 nm/pixel. The number in the upper right corner indicates the section index. Note the noticeable improvement in amount of non-linear distortion remaining in the elastically aligned series compared to the rigidly aligned series (**Supplementary Video 4**). A high resolution version of the movie can be downloaded from http://fly.mpi-cbg.de/elastic. The data can be interactively browsed in CATMAID at http://fly.mpi-cbg.de/c-elegans.
Supplementary Video 7	*Walk through the elastically aligned C. elegans series orthogonally re-sliced.* The movie shows in each frame a single, computationally generated section, orthogonal to the physical sectioning plane, through the elastically aligned TEM section series of a *C. elegans* three-fold stage embryo. Sections were down-sampled such that their lateral resolution matches the section thickness of 50 nm/pixel. Accordingly, orthogonal sections are generated at a step-size of 50 nm. The number in the upper right corner indicates the virtual section index. Two different zoom levels are shown (A,B) where B corresponds to the blue rectangle in A. The scale bars in the panels are 5 µm (A) and 2 µm (B). Note that the data have a familiar TEM appearance in the axial direction owing to the near complete removal of non-linear distortion by the elastic alignment method. A high resolution version of the movie can be downloaded from http://fly.mpi-cbg.de/elastic.
Supplementary Video 8	*Walk through the rigidly aligned Drosophila series.* The movie shows in each frame a single section from the rigidly aligned TEM section series, imaged as mosaic of overlapping tiles, of the *D. melanogaster* first instar larval ventral nerve cord at four different zoom levels (A-D where B shows the close up of the blue rectangled area in A etc.). The scale bars in each panel are 10 µm (A), 3 µm (B), 1 µm (C) and 0.5 µm (D). The lateral resolution of the raw data is 4 nm/pixel. The number in the upper right corner indicates the section index. Note the significant non-linear distortion remaining in the rigidly aligned data. A high resolution version of the movie can be downloaded from http://fly.mpi-cbg.de/elastic.
Supplementary Video 9	*Walk through the rigidly aligned Drosophila series orthogonally re-sliced.* The movie shows in each frame a single, computationally generated section, orthogonal to the physical sectioning plane, through the rigidly aligned TEM section series of the *D. melanogaster* first instar larval ventral nerve cord imaged as mosaic of overlapping tiles. Sections were down-sampled such that their lateral resolution matches the section thickness of 45 nm/pixel. Accordingly, orthogonal sections are generated at a step-size of 45 nm. The number in the upper right corner indicates the virtual section index. Two different zoom levels are shown (A,B) where B corresponds to the blue rectangle in A. The scale bars in the panels are 5 µm (A) and 3 µm (B). The lateral resolution of the raw data is equal to the section thickness that is

	45 nm/pixel. Note the strong non-linear distortion remaining in the rigidly aligned data that effectively prevents identification of biologically relevant features in the axial direction. A high resolution version of the movie can be downloaded from http://fly.mpi-cbg.de/elastic.
Supplementary Video 10	*Walk through the elastically aligned Drosophila series.* The movie shows in each frame a single section from the elastically aligned TEM section series, imaged as mosaic of overlapping tiles, of the *D. melanogaster* first instar larval ventral nerve cord at four different zoom levels (A-D where B shows the close up of the blue rectangled area in A etc.). The scale bars in each panel are 10 µm (A), 3 µm (B), 1 µm (C) and 0.5 µm (D). The lateral resolution of the raw data is 4 nm/pixel. The number in the upper right corner indicates the section index. Note the noticeable improvement in amount of non-linear distortion remaining in the elastically aligned series compared to the rigidly aligned series (**Supplementary Video 8**). A high resolution version of the movie can be downloaded from http://fly.mpi-cbg.de/elastic.
Supplementary Video 11	*Walk through the elastically aligned Drosophila series orthogonally resliced.* The movie shows in each frame a single, computationally generated section, orthogonal to the physical sectioning plane, through the elastically aligned TEM section series of the *D. melanogaster* first instar larval ventral nerve cord imaged as mosaic of overlapping tiles. Sections were down-sampled such that their lateral resolution matches the section thickness of 45 nm/pixel. Accordingly, orthogonal sections are generated at a step-size of 45 nm. The number in the upper right corner indicates the virtual section index. Two different zoom levels are shown (A,B) where B corresponds to blue rectangle in A. The scale bars in the panels are 5 µm (A) and 3 µm (B). Note that the data have a familiar TEM appearance in the axial direction owing to the near complete removal of non-linear distortion by the elastic alignment method. A high resolution version of the movie can be downloaded from http://fly.mpi-cbg.de/elastic.
Supplementary Video 12	*Rigid Alignment of an Array Tomography Series.* The movie shows a sample series of 43 serial sections of 70 nm thickness each from barrel cortex of an adult Line H YFP mouse18 expressing YFP in a subset of layer 5b pyramidal cells, pial surface at the top. Each section shows three fluorescent channels imaged by light microscopy as an aribitrary RGB overlay, DAPI (blue), YFP (green) and Synapsin (red). As with ssTEM data there is significant remaining non-linear distortion present in the rigidly aligned dataset. Data courtesy of Forrest Collman, Nick Weiler, Kristina Micheva and Stephen Smith.
Supplementary Video 13	*Elastic Alignment of an Array Tomography Series.* The movie shows a sample series of 43 serial sections of 70 nm thickness each from barrel cortex of an adult Line H YFP mouse18 expressing YFP in a subset of layer 5b pyramidal cells, pial surface at the top. Each section shows three fluorescent channels

	imaged by light microscopy as an aribitrary RGB overlay, DAPI (blue), YFP (green) and Synapsin (red). Analogously to ssTEM data, the elastic alignment removes most of the non-linear distortion from the light microscopy section series. Data courtesy of Forrest Collman, Nick Weiler, Kristina Micheva and Stephen Smith.
Supplementary Video 14	*3d rendering of elastically aligned Array Tomography Series.* Part of the elastically aligned dataset shown in **Supplementary Video 13** was used to generate a 3d volume rendering that demonstrates how well neuronal morphology can be reconstructed from the elastically aligned series. Data courtesy of Forrest Collman, Nick Weiler, Kristina Micheva and Stephen Smith.

EDITORIAL SUMMARY
A method for re-aligning images from serially sectioned biological specimens is described. The method minimizes the effect of artificial deformations in the alignment by applying global elastic constraints. It's applied to transmission Electron Microscopy and Array Tomography image series and it's made available through the Fiji platform.

Figure 1

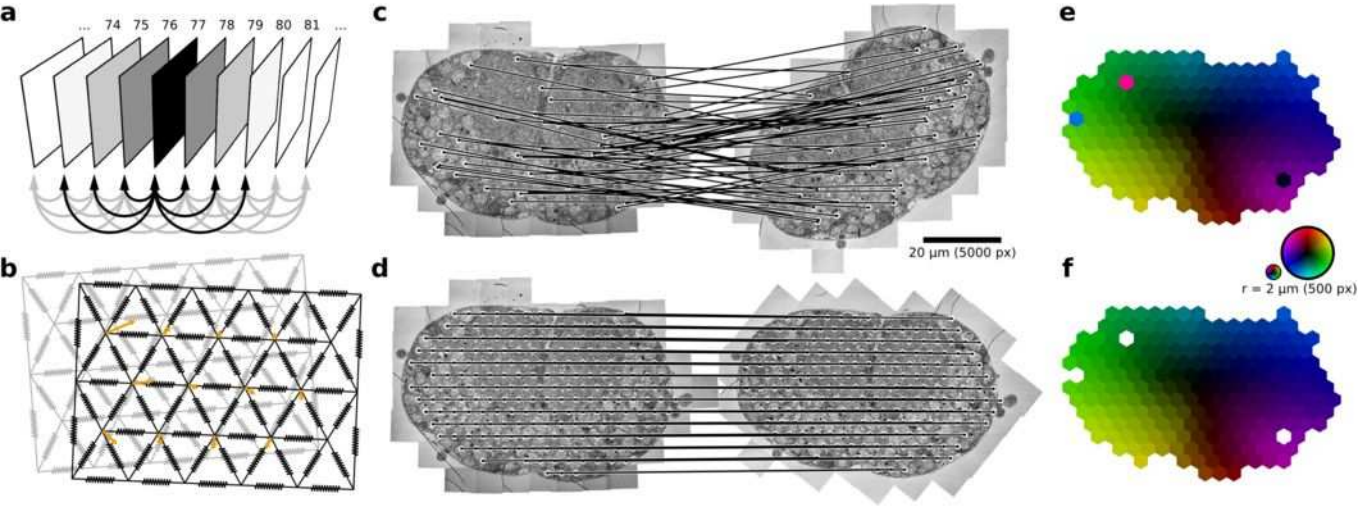

Figure 2

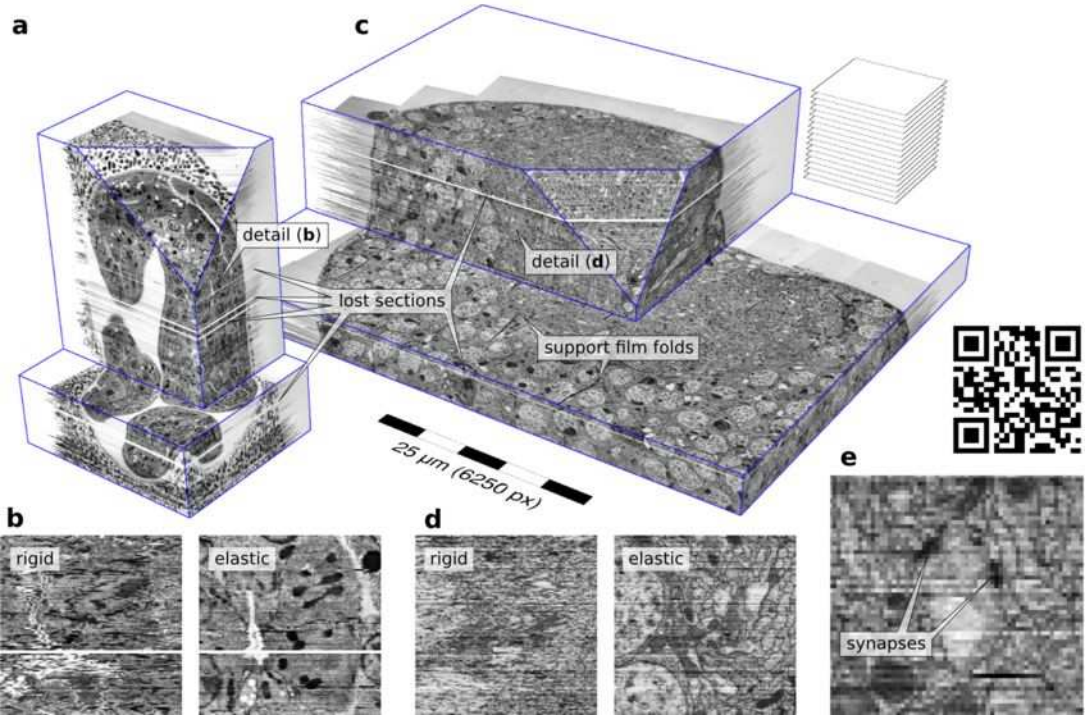
a
c
detail (b)
lost sections
detail (d)
support film folds
25 µm (6250 px)
b
rigid
elastic
d
rigid
elastic
e
synapses

Figure 3

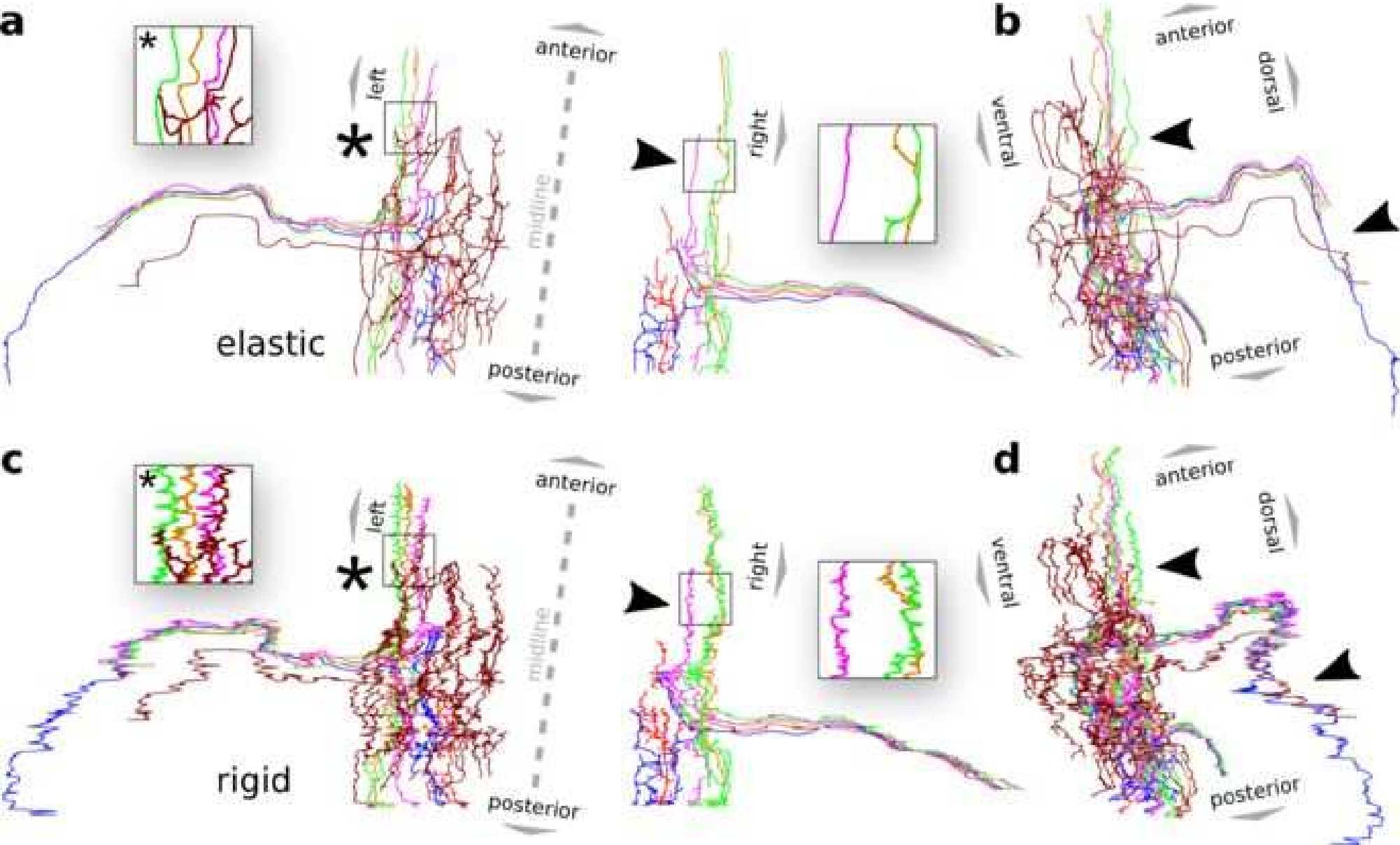
a
b
c
d
anterior
posterior
left
right
midline
dorsal
ventral
elastic
rigid

Supplementary Note

Triangle sizes

A triangle of springs has two families of cost minima in the plane: (1) at rigid transformations and (2) at rigid transformations flipped. That is, for all local deformations smaller than the size of a triangle, the mesh will drag towards a rigid transformation. For larger deformation, it may fold. The resolution of the triangle meshes should thus be chosen such that the expected local deformation does not exceed the side-length of a triangle.

The mesh resolution chosen for our experiments (24 in the C. elegans series and 48 in the Drosophila series) is a trade-off between alignment accuracy and execution speed. Since correspondences are searched for each vertex of the mesh by block matching, increasing the resolution of the mesh improves accuracy but increases runtime. Around discontinuities like section folds or tears, a region of up to the side-length of a triangle suffers from potentially inaccurate alignment. The error decreases with increasing distance to the discontinuity and reaches 'normal' values at the boundary to an adjacent triangle if for all its vertices a block match could be identified. Although our method in its present form does not explicitly model discontinuous deformation, it performs robustly in their presence. A discontinuous deformation in one section of a series will not compromise the alignment of the series because it will be overruled by all sections in their local neighborhood.

Regularized global affine alignment

In situations where only pairwise alignment is required (e.g. as initialization for block matching), higher order, less constrained transformation models can be used (e.g. an affine transformation). For groupwise alignment (series alignment or montaging), propagation of arbitrary scaling or shearing must be prevented. Using an unconstrained affine transformation in a global approach[8] has its optimum at a scale factor of zero. Using it sequentially would lead to increasing scale change and random shear (data not shown). We have therefore used a rigid transformation as a regularization term for the affine transformation which effectively prevents a global solution from introducing systematic shear and scale. Let **A** be an affine transformation and **R** be a rigid transformation. Both transformations are estimated by means of least-squares correspondence point displacement. The desired regularized affine transformation according to a regularization factor λ ranging between zero and one is then the linearly interpolated transformation $\mathbf{B}=(1-\lambda)\mathbf{A}+\lambda\mathbf{R}$. In our experiments, we have used a regularization factor $\lambda=0.1$ which proved a good tradeoff between regularization and the affine

transformation's ability to cope with non-rigid deformation.

Simultaneous alignment and recognition

Similar to the original application for robust object recognition[7], we use local image feature matches not only to align overlapping images but as well to identify overlapping images in non-initialized montages and to automatically estimate the range of sections in a series to be connected during elastic alignment (**Fig. 1a**). To that end, we match the features for each pair of images. Where no correspondences for two images could be identified, the conclusion can be drawn that they do not contain similar enough image content. When exploring non-initialized montages, all image pairs need to be analyzed. For identifying the range of sections to be compared in a series, we analyze pairs of increasing distance until matching has failed repeatedly. That way, the complexity of the comparison is greatly reduced while still offering the opportunity to bridge across artifactually distorted sections in the series. We have used this recognition capability to exclude empty and disconnected tiles from the *Drosophila* dataset. Out of 77,017 images, 33,499 images were automatically recognized as non-empty connected content and aligned, all other tiles were excluded from the dataset. We have later manually removed 448 tiles that were not showing parts of the specimen but were connected to section montages through texture from artifacts and background, resulting in 33,051 images all contributing to the reconstruction of the specimen.

Imaged datasets

We have applied our elastic alignment method to two outstanding ssTEM datasets (**Supplementary Table 1**) and one series of sections imaged by light microscopy. The C. elegans dataset showing a three-fold stage embryo was generated in 2003 by Richard Fetter in the laboratory of Cori Bargmann. The timed embryo collection was prepared by high pressure freezing and freeze-substitution. Sections were cut and imaged on a JEOL 1200EX TEM using Kodak 4489 film. The negatives were then digitized with an Epson flat bed scanner. Each negative was 3.25"×4" in physical size.

The *D. melanogaster* dataset showing 1.5 segments of the ventral nerve cord of a first instar larva was acquired by Richard Fetter and Albert Cardona at the Janelia Farm Research Campus using an FEI Tecnai T20 transmission EM electron microscope. Each section was imaged with a Gatan 895 4,096×4,096 pixels digital camera as a series of overlapping image tiles. Typically about 150 tiles were recorded per section. More than half of the acquired tiles, mostly on the periphery of the ventral nerve cord, lacked any image content and were automatically removed during the alignment procedure. During serial sectioning, inevitably, some sections are lost. For the *C.elegans* series this happened in

nine different places and for *Drosophila* it happened twice.

The light microscopy dataset has been generated using Array Tomography[15] by Forrest Collman, Nick Weiler, Kristina Micheva and Stephen Smith. In this method the tissue is sectioned into a series of ultra-thin sections achieving an axial resolution far beyond that of optical sectioning techniques. Each section is repeatedly stained with antibodies, imaged by light microscopy and destained. In this way it is possible to study co-localization of potentially many proteins in the same tissue. Our elastic method can be used to obtain the 3d reconstruction of the section series after each staining cycle. In the particular case shown in **Supplementary Videos 12–14** we reconstructed a sample series of 43 serial sections of 70 nm thickness each from barrel cortex of an adult Line H YFP mouse[20] expressing YFP in a subset of layer 5b pyramidal cells, pial surface at the top. Each section shows three fluorescent channels imaged by light microscopy as an arbitrary RGB overlay, DAPI (blue), YFP (green) and Synapsin (red). Interestingly, the 3d rendering (**Supplementary Video 14**)[21] reveals that given the ultra-thin sections and the limits of resolution imposed on light-microscopy, in this dataset, the axial resolution (70 nm) is better then the lateral one.

Implementation and Availability

We have implemented our method in the Java programming language. We have included it into our Open Source library (http://pacific.mpi-cbg.de/cgi-bin/gitweb.cgi?p=mpicbg.git) that we distribute with Fiji[14]. We provide two standalone plugins for Fiji. The plugin Elastic Stack Alignment takes a stack of images and aligns it as a section series. The stack can be virtualized such that only the necessary images for every step are loaded, allowing an off-the-shelf desktop computer to align very large series. The plugin Elastic Montage implements the automatic elastic registration of 2d image tiles, and is used for montaging mosaics from series of overlapping image tiles where the tiles have non-linear relative deformations. Tiles are provided as an unordered stack of images. The plugin estimates the configuration of the mosaic automatically. In addition, we integrated both elastic montaging and elastic series alignment into the TrakEM2 Open Source software included in Fiji[12]. TrakEM2 virtualizes access to all image tiles and provides an interactive point-and-click environment to montage or register subsets of the data and to manually alter the results of the automatic elastic registration. In TrakEM2 our elastic registration method complements many other tools to organize, align, adjust, segment, visualize and analyze large and small electron microscopy datasets (Cardona et al. manuscript in preparation). Each image can be transformed by a sequence of arbitrary transformations without degrading its quality by consecutive rendering steps. That is, elastic montaging and series alignment can be executed on image data that was previously corrected for lens-distortion[22] or pre-aligned using a different method[8]. Likewise, the elastically aligned series, individual images, or sections may be

deformed subsequently to correct for alignment errors or systematic distortion. This is of particular interest since the proposed image-based alignment method can compensate for independent section-deformation only and will preserve systematic distortion such as e.g. compression of the volume along the cutting direction.

All expensive independent operations are parallelized for optimal use of a single computer with multiple CPU cores accessing shared random access memory (RAM). Further scalability may be achieved by distributing the dominant operation: independent image-to-image pairwise block-matching and filtering to a cluster of independent computers with non-shared memory. To establish the required infrastructure for this is subject of future improvements of the implementation.

References

20. Feng et al. *Neuron* **28**(1), 41–51 (2000).
21. Schmid, B., Schindelin J., Cardona A., Longair M. and Heisenberg M. *BMC Bioinformatics* **11**: 274 (2010).
22. Kaynig, V., Fischer B., Müller E., and Buhmann J.M. *J Struct Biol* **171**(2):163–173 (2010).

Supplementary Figures

Supplementary Figure 1 | *Comparison of elastic alignment exploring eight adjacent sections or only direct neighbors.*

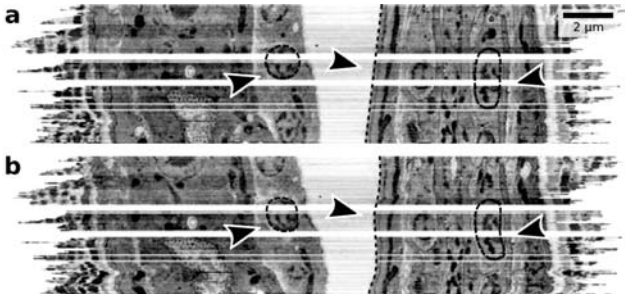

An axial virtual slice of a subset of sections through a three-fold stage *C. elegans* embryo (two parts of the same folded embryo are visible) that were aligned elastically connecting each section either to a local neighborhood of 8 sections (**a**) or only to its directly adjacent sections (**b**). Alignment using a larger local neighborhood (**a**) outperforms alignment where only direct neighbors were used (**b**); the nuclei adopt smooth oval shape even in the presence of missing sections (white bands across) and vertical features are continuous and straight (arrowheads). The apparently jagged edges on each side are the result of each section image covering a slightly different field of view at arbitrary orientation. In the aligned staple, images overlap only partially.

Supplementary Figure 2 | *Typical artifacts that inevitably occur in large TEM series.*

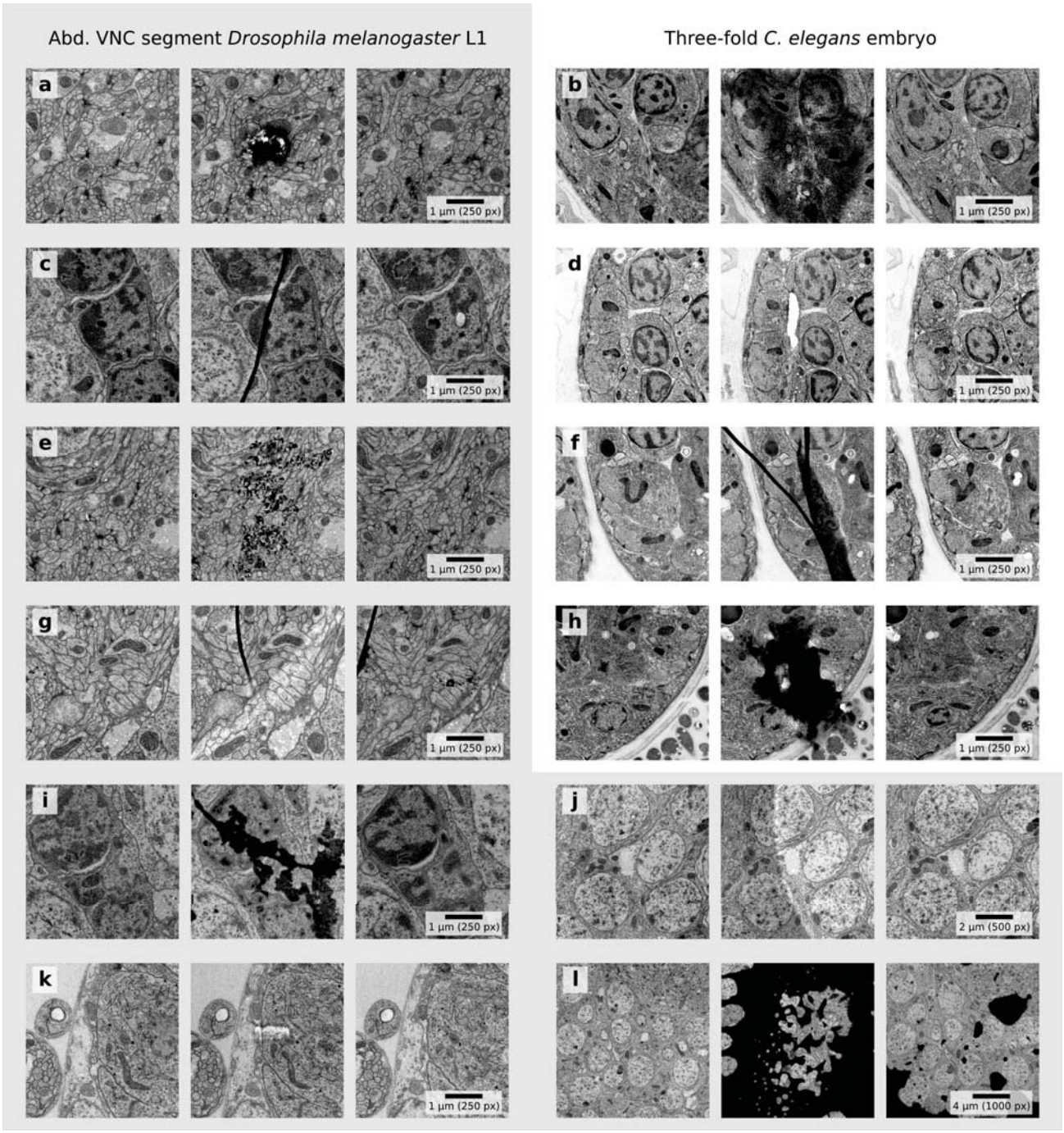

Snapshots of the elastically aligned *Drosophila* and *C. elegans* series show a section compromised by an artifact in context with adjacent sections. Some artifacts impact image similarity but have no effect on geometry (dirt (**a**,**h**), staining precipitates (**a**,**b**,**e**,**i**,**l**), support film folds (**f**,**g**,**i**), illumination variance (**g**,**j**). Others distort local geometry (section folds (**c**), stretches (**g**,**k**), cracks (**d**,**k**)).

Supplementary Figure 3 | *Local block matching filters*.

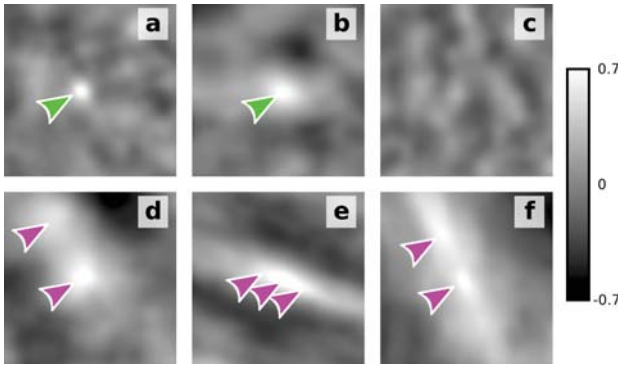

Shown is the NCC coefficient *r* of a block of a image *I*1 over a reference image *I*2 for all translational offsets in a square region with the coordinate origin in the center. Coefficients *r* are displayed as gray values (see scale). The candidate for the sought after translational offset is the location with maximal *r* (**a**,**b**). Candidates are rejected if either *r* was below a given threshold (**c**; not similar), there was more than one maximum with very similar *r* (**d**,**f**; ambiguous), or the maximum is not well localized in both dimensions (**e**,**f**; an edge pattern that fits everywhere alongside the edge).

Supplementary Figure 4 | *The number of filtered matches can be used to detect artifacts and missing sections.*

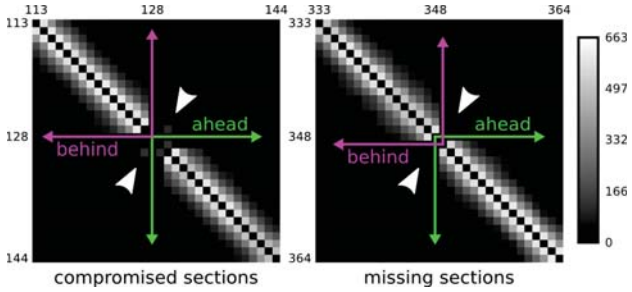

Shown are two areas along the diagonal cropped from an all to all matrix showing the number of matches that have passed the filters for each pair of sections from the *Drosophila* series. Numbers are encoded as gray values (see scale). Both panels show that the number of matches decreases with increasing distance of two sections in the series. The left panel shows the effect of two compromised sections (128 and 129) where more than 50% of the surface was covered with artifacts. Compromised sections will have a reduced number of matches with all sections behind and ahead in the series. Sections behind and ahead of the compromised sections generate the number of matches that corresponds to their relative distance (arrows). The right panel shows the effect of a gap of five sections between sections 348 and 349. The number of matches is consistently reduced for the section before the gap in forward direction and for the section after the gap in inverse direction (arrows).

Supplementary Figure 5 | *Spring forces.*

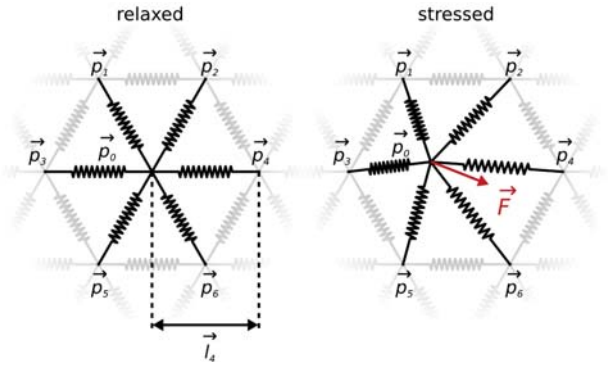

Each vertex p_0 is connected to other vertices p_i by an ideal spring. Each spring has a relaxed length l_i (shown for p_4). This relaxed length is zero for springs connecting to other images. The force of each spring can be calculated using Hooke's law summing up to the combined force vector F. The desired end-state of the system is where $F = 0$ for all vertices.

Supplementary Figure 6 | *Elastic montaging compensates for non-rigid deformation.*

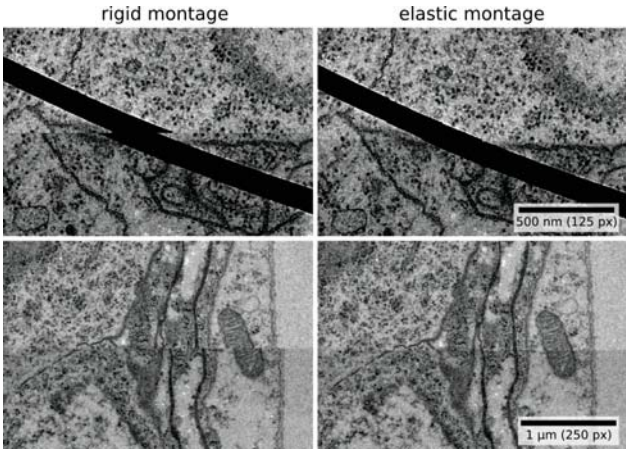

Lens distortion effects and heat-induced deformation of sections during imaging renders montaging with a rigid transformation per tile insufficient. Only an elastic approach can compensate for non-linear tile-to-tile distortion while minimizing the non-rigid deformation simultaneously. Note that the shown stitching errors do not result from non-optimal rigid alignment but exclusively from non-rigid deformation.

Supplementary Figure 7 | *Comparison of average section scale factors after alignment of the evaluation series.*

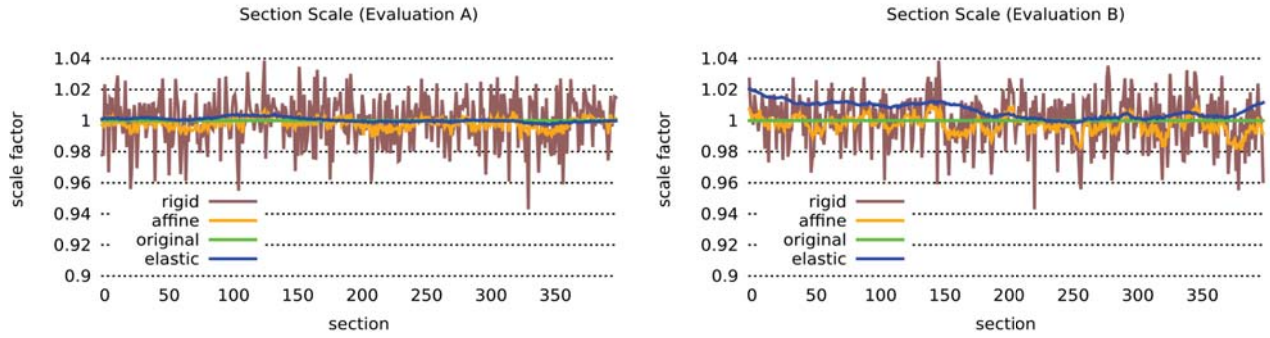

The average scale factor of a section relative to the non-deformed ground-truth is estimated through a least-squares approximation of the artificially introduced non-linear deformation by a similarity transformation (scale, rotation, translation). Since non-linear deformation has been introduced to all sections independently, no systematic scale change is expected across the series. All three methods preserve this property (**Supplementary Videos 2** and **3**). Elastic alignment almost perfectly recovers the original scale of all sections. As expected, the performance is better for series A where no signal change compromises the measured motion vectors.

Supplementary Figure 8 | *Histograms of absolute point displacements after alignment of evaluation series A and B.*

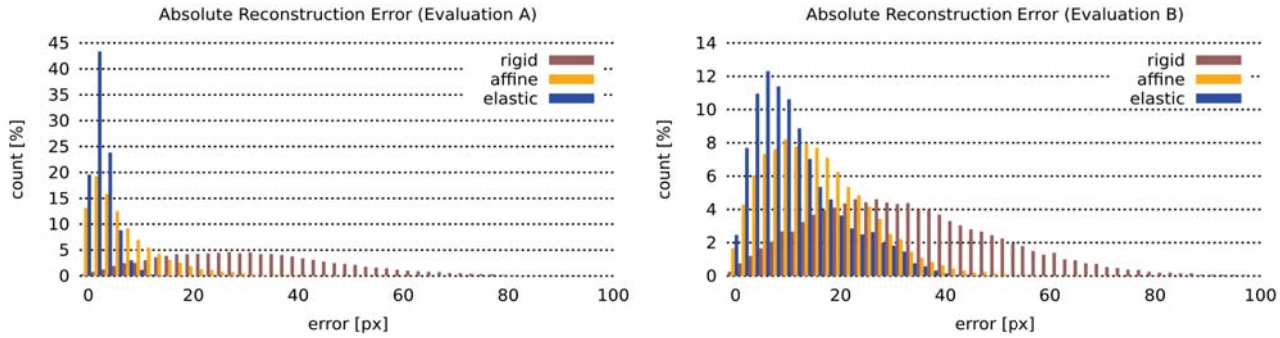

We have measured the absolute displacement in the *x*,*y*-plane relative to ground truth of each *z*-point of a sample of straight lines projected through the volume along the *z*-axis. Elastic alignment outperforms both methods. As expected, the result is slightly better in evaluation series A where no signal change compromises the measured motion vectors (left graph).

Supplementary Figure 9 | *Projection of the x,y-location of each z-point of a sample of straight lines projected through the volume along the z-axis*.

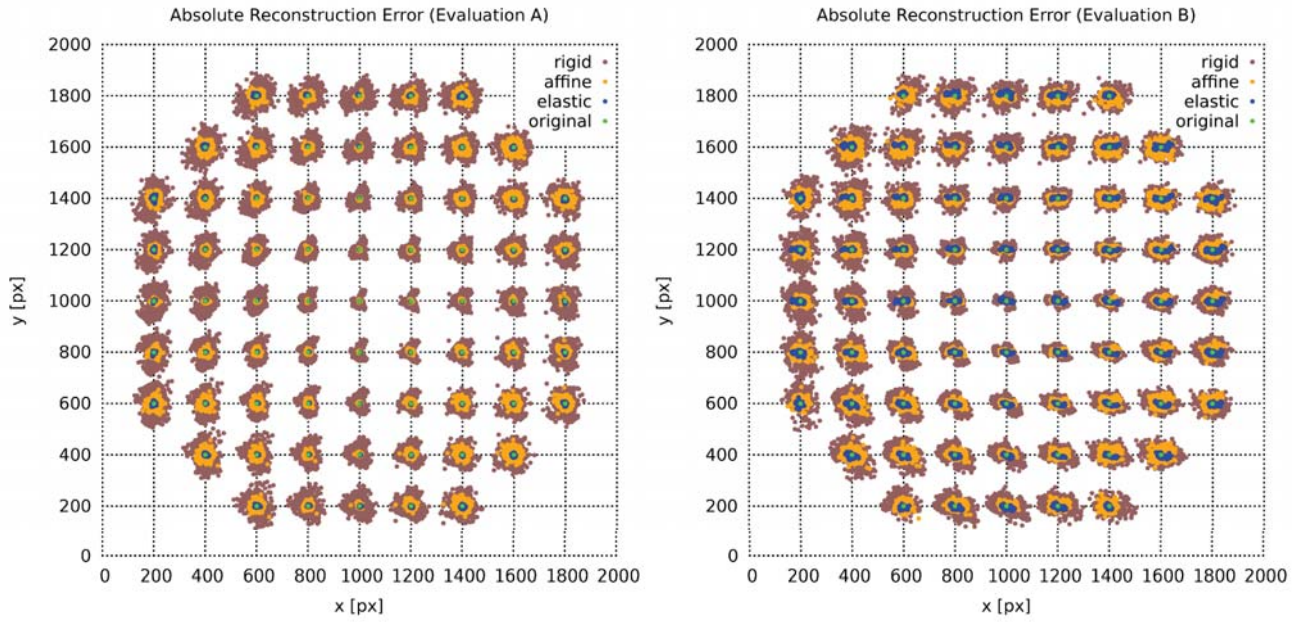

Elastic alignment very well recovers the original location of all points along the lines. As expected, the result is slightly better in evaluation series A where no signal change compromises the measured motion vectors (left graph). The displacement is minimal in the center of the volume and increases towards the periphery for all methods used. This effect is comparatively minimal in case of the elastic alignment.

Supplementary Figure 10 | *Projection of the x,z-location of each z-point of a sample of straight lines projected through the volume along the z-axis*.

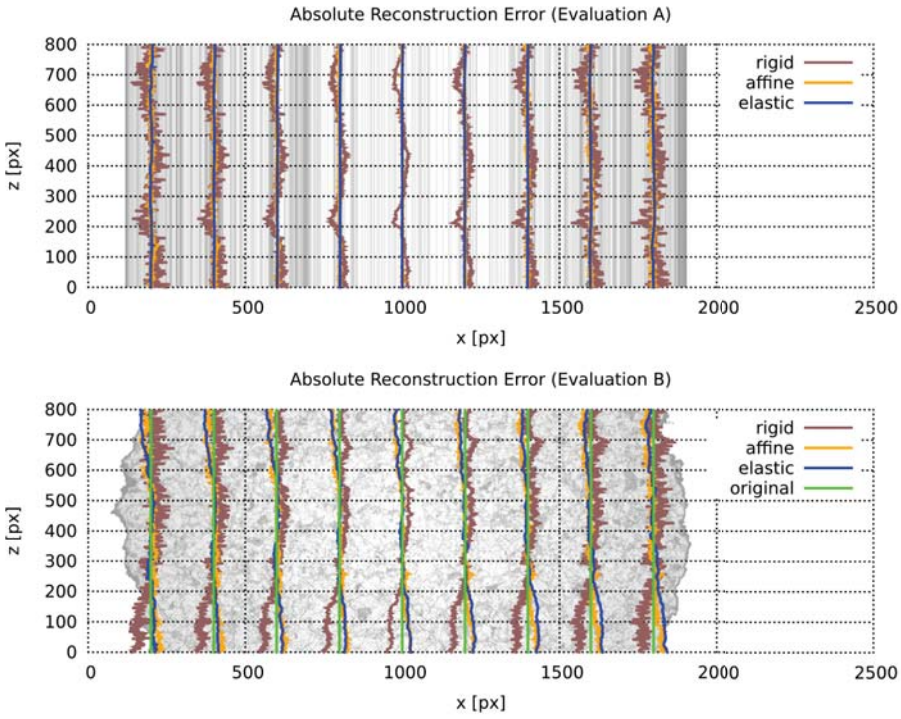

Elastic alignment very well recovers the original location of all points along the lines. As expected, the result is slightly better in evaluation series A where no signal change compromises the measured motion vectors (top graph). The displacement is minimal in the center of the volume and increases towards the periphery for all methods used. This effect is comparatively minimal in case of the elastic alignment. The background of the plot shows the corresponding *x*,*z*-section of the respective original evaluation series (note that in the top graph the texture of the volume does not change along the *z*-axis as all sections are the same).

Supplementary Figure 11 | *Histograms of section-to-section pairwise point displacements after alignment of evaluation series A and B.*

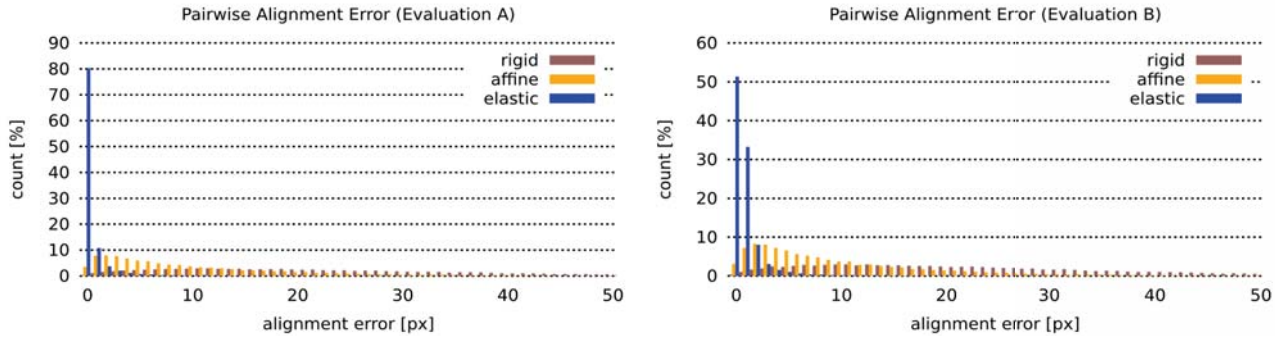

We have measured the pairwise displacement in the *x*,*y*-plane between adjacent sections for a sample of straight lines projected through the volume along the *z*-axis. Elastic alignment outperforms both linear methods significantly. As expected, the result is better in evaluation series A where no signal change compromises the measured motion vectors (left graph). Note that in evaluation series A for 80% of all sampled locations the pairwise displacement is below 1 pixel and for 90% below 2 pixel. In evaluation series B for 50% of all sampled locations the pairwise displacement is below 1 pixel and for 80% it is below 2 pixel.

Supplementary Figure 12 | *Visualization of section-to-section pairwise point displacements after alignment of evaluation series A and B.*

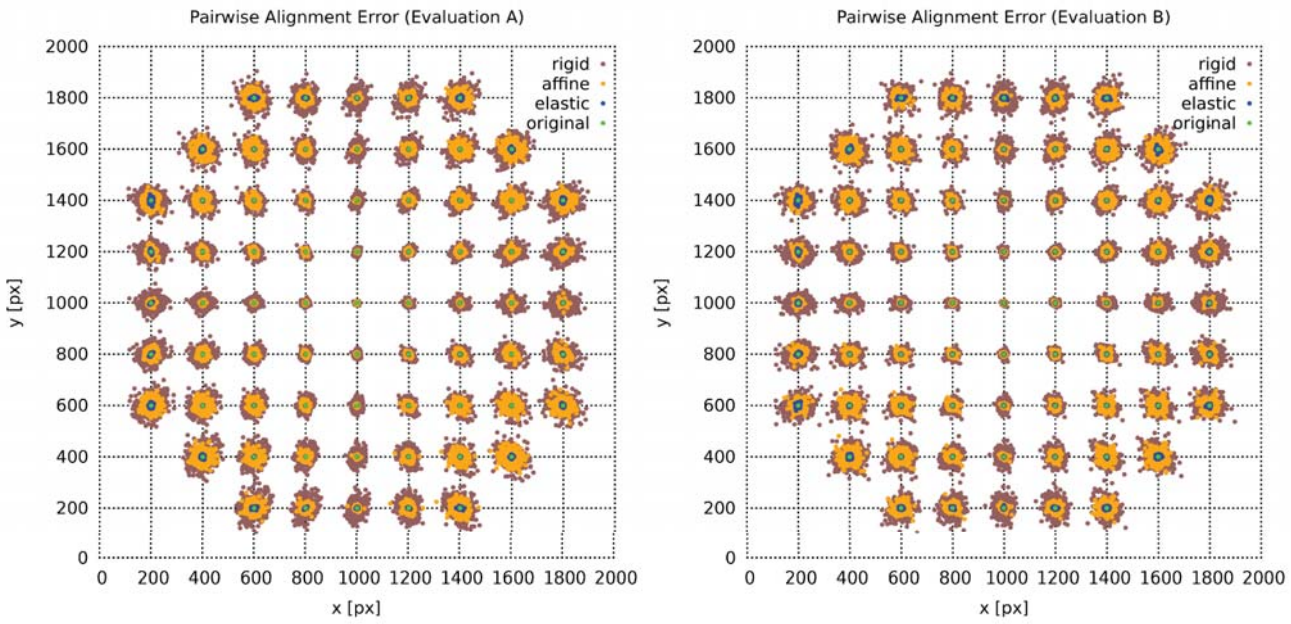

The pairwise displacement for each *z*-point of a sample of straight lines projected through the volume along the z-axis are displayed centered at the original *x*,*y*-location of the corresponding line. Elastic alignment outperforms both linear methods significantly. As expected, the result is better in evaluation series A where no signal change compromises the measured motion vectors (left graph). The pairwise displacement is minimal in the center of the volume and increases towards the periphery for all methods used. This effect is comparatively minimal in case of the elastic alignment.

Supplementary Figure 13 | *Anatomical context of Drosophila larval ventral nerve cord ssTEM.*

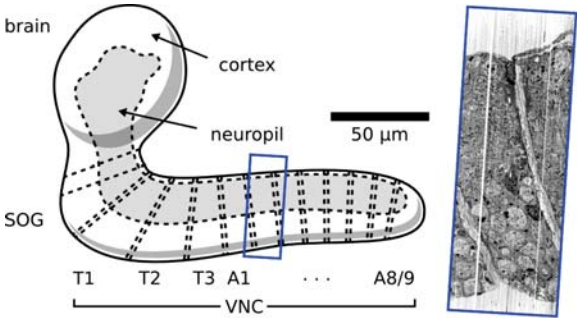

Cartoon based on a figure from Ito et al. 1995[19]. The blue box marks the approximate area from which the series of sections originates (note that the exact location of the series within abdominal segments is not known). The inset shows the sagital plane at the midline through the elastically aligned volume. VNC - ventral nerve cord, SOG - subesophageal ganglion, T1–3 - thoracic segments, A1–9 - abdominal segments.

Supplementary Figure 14 | *Synapses are detectable in both lateral and axial views after elastic reconstruction.*

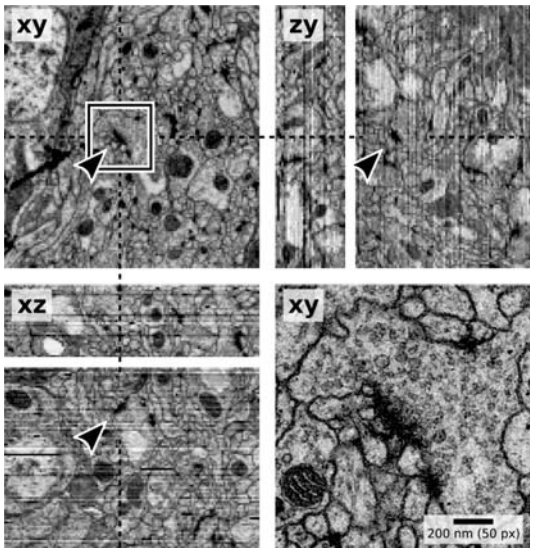

A synapse (arrowheads) is shown in lateral (**xy**) and two axial (**zy, xz**) views of the elastically aligned *Drosophila* dataset. The top left lateral and both axial views were generated from the section series scaled down to isotropic resolution. The area highlighted by a black square is shown at the original lateral resolution of 4nm/px (**xy**, bottom right). While single vesicles can be distinguished only in the high resolution image of the section, it is possible to identify synapses by their increased pre-synaptic density at axial resolution. The white bands visible in the axial panels are missing sections. The dashed lines indicate the locations of the respective axial sections.

Supplementary Figure 15 | *Comparison of three alignment methods applied to the Drosophila series using the total length of manual skeleton annotation.*

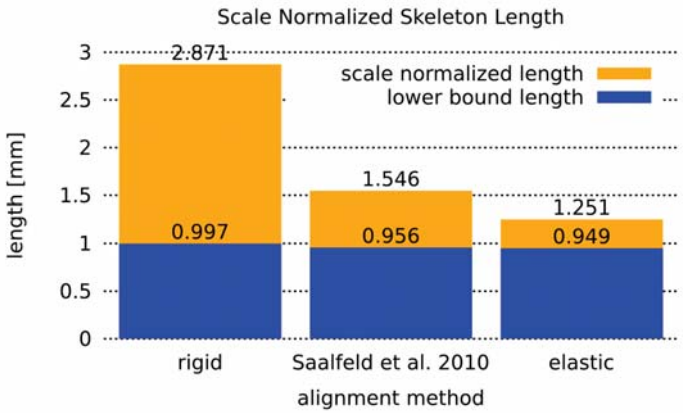

The first method is a sequential alignment using a rigid transformation per section estimated from automatically extracted features (rigid). The second method estimates a rigid transformation per each mosaic tile globally minimizing the total square displacement of automatically extracted feature correspondences (Saalfeld et al. 2010)[8]. The third is our new elastic method initialized with the result of the second method. We report the total length of manually traced neuronal arbor skeletons with all edge lengths normalized by a local scale factor *s* (**Equation 3**). The local scale factor *s* for each skeleton edge (*p*,*q*) is the average scale factor of the contributing sections at *p* and *q* relative to the original image size. We compare the total skeleton length with an approximate lower bound skeleton length calculated from all edges between branch and end nodes of the skeleton replaced by straight lines (**Supplementary Fig. 16**).

Supplementary Figure 16 | *Total skeleton length and lower bound skeleton length.*

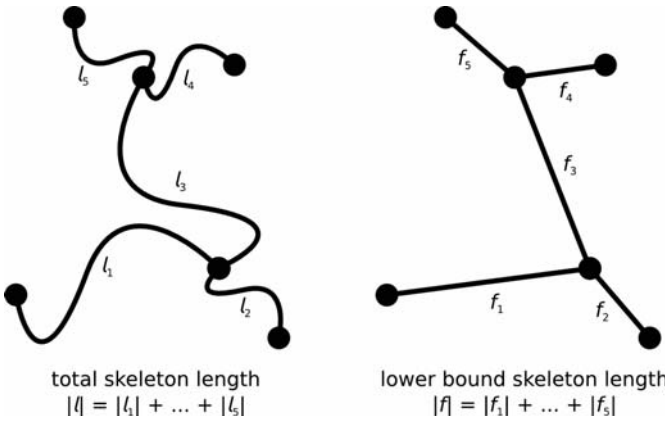

We compare the total skeleton length *l* with a lower bound skeleton length *f* that serves as an approximation of the minimal possible skeleton length and is robust with respect to alignment errors. The lower bound length *f* is the sum of the length of all edges between branch and end points of the skeleton replaced by straight lines.

Supplementary Note

Triangle sizes

A triangle of springs has two families of cost minima in the plane: (1) at rigid transformations and (2) at rigid transformations flipped. That is, for all local deformations smaller than the size of a triangle, the mesh will drag towards a rigid transformation. For larger deformation, it may fold. The resolution of the triangle meshes should thus be chosen such that the expected local deformation does not exceed the side-length of a triangle.

The mesh resolution chosen for our experiments (24 in the C. elegans series and 48 in the Drosophila series) is a trade-off between alignment accuracy and execution speed. Since correspondences are searched for each vertex of the mesh by block matching, increasing the resolution of the mesh improves accuracy but increases runtime. Around discontinuities like section folds or tears, a region of up to the side-length of a triangle suffers from potentially inaccurate alignment. The error decreases with increasing distance to the discontinuity and reaches 'normal' values at the boundary to an adjacent triangle if for all its vertices a block match could be identified. Although our method in its present form does not explicitly model discontinuous deformation, it performs robustly in their presence. A discontinuous deformation in one section of a series will not compromise the alignment of the series because it will be overruled by all sections in their local neighborhood.

Regularized global affine alignment

In situations where only pairwise alignment is required (e.g. as initialization for block matching), higher order, less constrained transformation models can be used (e.g. an affine transformation). For groupwise alignment (series alignment or montaging), propagation of arbitrary scaling or shearing must be prevented. Using an unconstrained affine transformation in a global approach[8] has its optimum at a scale factor of zero. Using it sequentially would lead to increasing scale change and random shear (data not shown). We have therefore used a rigid transformation as a regularization term for the affine transformation which effectively prevents a global solution from introducing systematic shear and scale. Let **A** be an affine transformation and **R** be a rigid transformation. Both transformations are estimated by means of least-squares correspondence point displacement. The desired regularized affine transformation according to a regularization factor λ ranging between zero and one is then the linearly interpolated transformation $\mathbf{B}=(1-\lambda)\mathbf{A}+\lambda\mathbf{R}$. In our experiments, we have used a regularization factor $\lambda=0.1$ which proved a good tradeoff between regularization and the affine transformation's ability to cope with non-rigid deformation.

Simultaneous alignment and recognition

Similar to the original application for robust object recognition[7], we use local image feature matches not only to align overlapping images but as well to identify overlapping images in non-initialized montages and to automatically estimate the range of sections in a series to be connected during elastic alignment (**Fig. 1a**). To that end, we match the features for each pair of images. Where no correspondences for two images could be identified, the conclusion can be drawn that they do not contain similar enough image content. When exploring non-initialized montages, all image pairs need to be analyzed. For identifying the range of sections to be compared in a series, we analyze pairs of increasing distance until matching has failed repeatedly. That way, the complexity of the comparison is greatly reduced while still offering the opportunity to bridge across artifactually distorted sections in the series. We have used this recognition capability to exclude empty and disconnected tiles from the *Drosophila* dataset. Out of 77,017 images, 33,499 images were automatically recognized as non-empty connected content and aligned, all other tiles were excluded from the dataset. We have later manually removed 448 tiles that were not showing parts of the specimen but were connected to section montages through texture from artifacts and background, resulting in 33,051 images all contributing to the reconstruction of the specimen.

Imaged datasets

We have applied our elastic alignment method to two outstanding ssTEM datasets (**Supplementary Table 1**) and one series of sections imaged by light microscopy. The C. elegans dataset showing a three-fold stage embryo was generated in 2003 by Richard Fetter in the laboratory of Cori Bargmann. The timed embryo collection was prepared by high pressure freezing and freeze-substitution. Sections were cut and imaged on a JEOL 1200EX TEM using Kodak 4489 film. The negatives were then digitized with an Epson flat bed scanner. Each negative was 3.25"×4" in physical size.

The *D. melanogaster* dataset showing 1.5 segments of the ventral nerve cord of a first instar larva was acquired by Richard Fetter and Albert Cardona at the Janelia Farm Research Campus using an FEI Tecnai T20 transmission EM electron microscope. Each section was imaged with a Gatan 895 4,096×4,096 pixels digital camera as a series of overlapping image tiles. Typically about 150 tiles were recorded per section. More than half of the acquired tiles, mostly on the periphery of the ventral nerve cord, lacked any image content and were automatically removed during the alignment procedure. During serial sectioning, inevitably, some sections are lost. For the *C.elegans* series this happened in nine different places and for *Drosophila* it happened twice.

The light microscopy dataset has been generated using Array Tomography[15] by Forrest Collman, Nick Weiler, Kristina Micheva and Stephen Smith. In this method the tissue is sectioned into a series of ultra-thin sections achieving an axial resolution far beyond that of optical sectioning techniques. Each section is repeatedly stained with antibodies, imaged by light microscopy and destained. In this way it is possible to study co-localization of potentially many proteins in the same tissue. Our elastic method can be used to obtain the 3d reconstruction of the section series after each staining cycle. In the particular case shown in **Supplementary Videos 12–14** we reconstructed a sample series of 43 serial sections of 70 nm thickness each from barrel cortex of an adult Line H YFP mouse[20] expressing YFP in a subset of layer 5b pyramidal cells, pial surface at the top. Each section shows three fluorescent channels imaged by light microscopy as an arbitrary RGB overlay, DAPI (blue), YFP (green) and Synapsin (red). Interestingly, the 3d rendering (**Supplementary Video 14**)[21] reveals that given the ultra-thin sections and the limits of resolution imposed on light-microscopy, in this dataset, the axial resolution (70 nm) is better then the lateral one.

Implementation and Availability

We have implemented our method in the Java programming language. We have included it into our Open Source library (http://pacific.mpi-cbg.de/cgi-bin/gitweb.cgi?p=mpicbg.git) that we distribute with Fiji[14]. We provide two standalone plugins for Fiji. The plugin Elastic Stack Alignment takes a stack of images and aligns it as a section series. The stack can be virtualized such that only the necessary images for every step are loaded, allowing an off-the-shelf desktop computer to align very large series. The plugin Elastic Montage implements the automatic elastic registration of 2d image tiles, and is used for montaging mosaics from series of overlapping image tiles where the tiles have non-linear relative deformations. Tiles are provided as an unordered stack of images. The plugin estimates the configuration of the mosaic automatically. In addition, we integrated both elastic montaging and elastic series alignment into the TrakEM2 Open Source software included in Fiji[12]. TrakEM2 virtualizes access to all image tiles and provides an interactive point-and-click environment to montage or register subsets of the data and to manually alter the results of the automatic elastic registration. In TrakEM2 our elastic registration method complements many other tools to organize, align, adjust, segment, visualize and analyze large and small electron microscopy datasets (Cardona et al. manuscript in preparation). Each image can be transformed by a sequence of arbitrary transformations without degrading its quality by consecutive rendering steps. That is, elastic montaging and series alignment can be executed on image data that was previously corrected for lens-distortion[22] or pre-aligned using a different method[8]. Likewise, the elastically aligned series, individual images, or sections may be deformed subsequently to correct for alignment errors or systematic distortion. This is of particular interest since the proposed image-based alignment method can compensate for independent section-

deformation only and will preserve systematic distortion such as e.g. compression of the volume along the cutting direction.

All expensive independent operations are parallelized for optimal use of a single computer with multiple CPU cores accessing shared random access memory (RAM). Further scalability may be achieved by distributing the dominant operation: independent image-to-image pairwise block-matching and filtering to a cluster of independent computers with non-shared memory. To establish the required infrastructure for this is subject of future improvements of the implementation.

References

20. Feng et al. *Neuron* **28**(1), 41–51 (2000).
21. Schmid, B., Schindelin J., Cardona A., Longair M. and Heisenberg M. *BMC Bioinformatics* **11**: 274 (2010).
22. Kaynig, V., Fischer B., Müller E., and Buhmann J.M. *J Struct Biol* **171**(2):163–173 (2010).

Supplementary Tables

Supplementary Table 1 | *Overview of reconstructed ssTEM datasets.*

	C. elegans three-fold stage embryo	*D. melanogaster* first instar larva ventral nerve cord
TEM recording mode	scanned from film	digital imaging of overlapping tiles
Number of sections	803	458
Image tiles per section	1	>70
Tile size	6,160×4,640	2,048×2,048 pixels
Bits per pixel	8	16
Section canvas size	6,160×4,640	~22,000×17,000 pixels
Lateral resolution	4 nm/pixel	4 nm/pixel
Section thickness	50 nm	45 nm
Missing sections	25*	2 + 5
Total number of images	803	33,051 (with content) 77,017 total**
Size in GB	21	258 (with content) 602 total*
Processing time	~ 12 hours	~ one week

*The record of the series declares missing sections at 9 different places, ranging from 1 up to 7 sections missing. Without knowing that in prior, we were able to identify the four larger gaps and their approximate sizes by analyzing the ratio of block matches that passed local and global filters (**Supplementary Fig. 4**). **Many tiles imaged on the periphery of the specimen contain only background. Our previously published feature based method8 explicitly removes these from the alignment because no corresponding image context can be found between images within and/or across sections.